Planetary Imaging Fourier Transform Spectrometer (PIFTS)

Final Report on NASA Grant NAG5-6248

Performance Period: 8 January 1997 - 31 July 2001

Principal Investigator: L.A. Sromovsky

University of Wisconsin - Madison
Space Science and Engineering Center
1225 West Dayton Street
Madison, WI 53706

19 February 2002

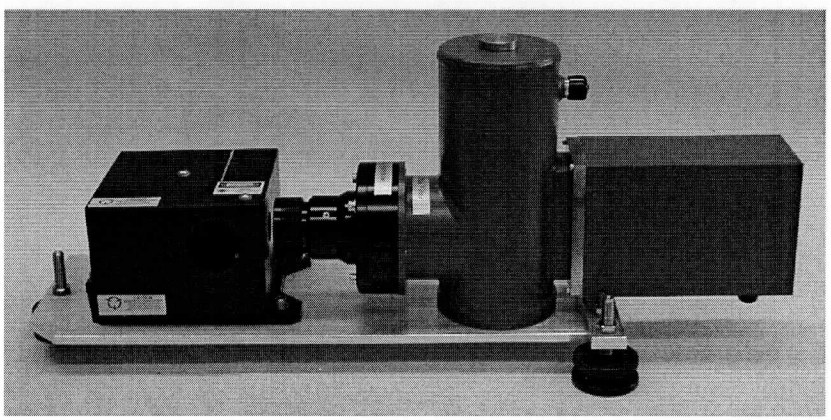

Project 6600

Contents

1 Introduction

This report describes efforts to design, build, and evaluate a breadboard of a Planetary Imaging Fourier Transform Spectrometer (PIFTS) for near-IR (1-5.2 μm) imaging of planetary targets with spectral resolving powers of several hundred to several thousand, using an InSb detector array providing at least 64×64 pixels imaging detail. The major focus of the development effort was to combine existing technologies to produce a small and low power design compatible with a very low mass flyable instrument. Efforts to date have shown great promise for the instrument concept, with potential for compositional mapping of planetary surfaces using reflected sunlight, thermal mapping using emitted radiation, as well as atmospheric investigations using near infrared gaseous absorption bands and windows to probe atmospheric opacity structure. We now have a working PIFTS breadboard and a preliminary evaluation of its performance characteristics, and have identified areas that need further evaluation and refinement before feasibility as a flight instrument can be demonstrated. In the following we first describe the organization and schedule of development, then the design details, test results, what remains to be done to make PIFTS a viable flight instrument, and potential science applications.

2 Breadboard Development Effort

With participation of Lockheed Martin Corporation (LMC), Denver CO, we carried out ray-tracing and performance analyses to specify the detailed configuration requirements for the interferometer and a detailed specification for the camera system. Bomem of Quebec, Canada, was contracted to construct the miniaturized interferometer and the detector and readout electronics were procured as an IR camera system from Santa Barbara Focal Plane of Goleta, California.

2.1 Original program plans

The enabling technologies we proposed to combine were 1) a voice coil drive used for interferometer mirror control, 2) an InSb infrared focal plane array as is used in IR cameras, 3) corner-cube retroreflectors used to reduce alignment sensitivity in laboratory instruments, 4) a small visible laser source and detector for controlling and measuring delay scan motion, and 5) a very small Stirling-cycle cryogenic cooler. We had planned to use a fixed corner cube and a linearly driven moving corner cube. As originally conceived, the University of Wisconsin Space Science and Engineering Center would have subcontracted to Lockheed Martin Astronautics (LMA) Space Systems Technology Development Department, for much of the breadboard design and testing. This planned division of labor and other implementation details have been modified to minimize development risks, as described in the next section.

2.2 Modifications of planned effort

Given the imminent retirement of the LMA interferometer expert (Bill Bloomquist), and the realization that our budget constraints required absolute minimal development risk, we decided to procure the basic interferometer subsystem from an experienced and well respected commercial vendor (Bomem), basing our miniaturized design on one of their very successful commercial instruments, rather than develop the interferometer subsystem at LMA. The full scale version of the Bomem instrument is a very familiar one at SSEC, as it serves as the basis for our Advanced Emitted Radiance Interferometer (Revercomb *et al.* 1994) that has seen wide

field use in the DOE Atmospheric Radiation Measurement (ARM) program. We took a similar philosophy in securing a working detector array. Instead of using LMA-designed readout electronics with a commercial focal plane assembly, we decided to procure a complete working IR camera system, including focal plane array, readout electronics, interfaced to a Pentium-based computer system, with software to control the array exposure and readout, as well as storage and processing of the raw image frames. Although this plan greatly enhances the predictability of the breadboard development, it was clear that the cost was still a significant issue, and we thus sought help with the camera procurement from a parallel project at SSEC that would benefit from the experience with test data from the PIFTS breadboard. The project is part of the NASA LaRC Advanced Geostationary Studies Program for developing an imaging FTS for temperature and water vapor sounding for operational weather applications. We also decided that we could not afford to include a Stirling-cycle cooler as part of the IR focal plane procurement. The cooler we had greatest confidence in using, partly because of its successful use in a non-imaging interferometer system, was not available with the commercial camera systems that met our other requirements, and the one that was available would cost an additional $15K. We decided that the added cost was not affordable, and brought some added risk as well, given no track record for that particular cooler in interferometer applications. Thus we selected an LN2 dewar for the breadboard.

2.3 Project Initiation

We were notified on 26 September 1997 of PIDDP funding for the period 8-1-97 through 7-31-98. We began planning for a kick-off meeting at Lockheed Martin Astronautics, and reviewed objectives, schedule, funding, and capabilities of participants. The kickoff meeting was held on Friday, 12 Dec 1997 at LMA on the outskirts of Denver, Colorado. Attendees included Joe Martin, Jack Eastman, and Scot Anderson from LMA, Larry Sromovsky (PI), Hank Revercomb, and Fred Best from the SSEC, and Martin Chamberland from Bomem. At the time of this meeting the Bomem PO was already released, and the LMA contract was in process at University Research Administration. The initial miniaturized Bomem design for the interferometer assembly was presented and key interface issues were discussed: (1) optical delay scan rates that were needed by the interferometer scan drive in comparison with the maximum possible image frame rate of the camera readout system, (2) triggering of detector integration timing using interferometer reference laser fringe measurements, (3) vignetting of the camera lens FOV by interferometer components. The initial survey of camera vendors revealed few that could provide true snap-shot exposure capability (for which all elements of the detector array start and stop exposures simultaneously), external triggering, and high radiometric performance. Action items following the meeting included (1) ray tracing of commercial camera lenses to define which parts of the interferometer needed to be adjusted to minimize vignetting, assigned to LMA; (2) revision of interferometer design details to account for ray tracing results, assigned to Bomem; (3) detailed definition of camera system capabilities, verification of feasibility of sampling requirements, and camera procurement, shared by LMA and UW, (4) performance analysis estimates for a variety of mission opportunities, as a sanity check on the breadboard design parameter choices, assigned to UW. Progress was tracked with email, telecons, and one additional visit to LMA in April.

2.4 Program Milestones and Schedule

The following is a list of key events and corresponding dates in the PIFTS development effort:

26 Sep 1997	Notification of funding.
14 Nov 1997	Verbal approval from Lori Moore, our PIDDP grant negotiator allowing us to reprogram funds from subcontract to capital equipment so that we could procure a commercial interferometer subsystem instead of develop it at Lockheed Martin.
5 Dec 1997	Initiate subcontract to Lockheed-Martin for PIFTS support effort.
12 Dec 1997	Kickoff Meeting at Lockheed-Martin.
16 Dec 1997	Release of PO for Bomem interferometer subsystem.
7 Aug 1998	On site visit to Santa Barbara Focal Plane by L. Sromovsky, H. Revercomb, D. La Porte, and R. Garcia of the University of Wisconsin.
18 Sep 1998	Request for bids issued by UW for providing IR imaging camera system.
26 Oct 1998	Release PO for IR camera system to Santa Barbara Focal Plane.
23 Nov 1998	Lens delivery by Diversified Optics.
3 Feb 1999	IR camera system shipped to UW by Santa Barbara Focal Plane.
4 May 1999	Camera functional checkout at UW. Resulted in return of camera to SBFP.
7 May 1999	Camera returned with repaired solder bond on focal plane.
6 Aug 1999	Camera returned to SBFP for repair of external synch triggering problems.
18 Aug 1999	Repaired camera returned from SBFP to UW.
17 Sep 1999	Shipment of BOMEM interferometer subsystem to Madison.
23 Sep 1999	Successful interferometer subsystem functional checkout shows it to be operational.
22 Oct 1999	First integrated system spectral observations of the atmosphere.
10 Feb 2000	Presentation of PIFTS paper at BOMEM workshop in Quebec.
9 Oct 2000	Presentation of PIFTS paper at SPIE conference in Japan.
25 Oct 2000	Completed image aquisition software to permit tighter integration of capture and triggering functions.
21 Nov 2000	First attempted intercomparison with AERI (weather interfered).

2.5 Project Expenditure Summary

EXPENDITURE	DESCRIPTION OF ITEM OR ACTIVITY
$226,724	UW Effort to manage program, carry out system design, specify subsystem requirements, procure subsystems, define and monitor subcontractor efforts, integrate and debug subsystems, conduct performance tests and analyses, and communicate and publish results.
$81,656	Subcontract to Lockheed-Martin Astronautics of Denver, CO, for advice on IR detector/camera selection, optical ray trace analysis, evaluation of readout electronics, and system design analysis.
$96,620	Interferometer subsystem procured from BOMEM.
$65,000	IR camera subsystem procured from Santa Barbara Focalplane of Goleta, CA. (Not payed for by PIDDP program.)

2.6 Interferometer Subsystem Procurement

The interferometer subsystem was procured from Bomem for a fixed price of $96,620. The interferometer PO was released in October 1998, but delivery was delayed somewhat beyond the expected delivery in July 1999, until late September 1999. Bomem made excellent progress in constructing the interferometer subsystem, but experienced unexpected difficulties with the scan drive servo system. The PIFTS requires a much slower scan rate then their commercial systems, requiring use of a new servo design that has took longer than anticipated to get functioning at the desired level of stability. In spite of this difficulty, Bomem delivered a fully functional system within the originally agreed-to budget. The current configuration of the interferometer mechanism and electronics are illustrated in the photographs of Figs. 2 and 3. While the interferometer mechanism and optics are miniaturized, the electronics are not (as evident in Fig. 3).

2.7 The PIFTS Camera System Procurement and Checkout

The bidders package for the IR camera system was released, and the selected vendor among two responsive bidders, was Santa Barbara Focalplane. The camera (delivered on 4 May 1999) is a commercial unit, model SYS-128S-1 ImagIR Camera System. The camera uses an InSb array of 320x256 pixels, providing a 128x128 subarray of 99.5% operable pixels, snapshot readout at 60-Hz frame rates, adjustable windowing to 128x64 and smaller subarrays that can be read at $>$ 1 kHz frame rates, user replaceable cold filter, detector response from 1-5 microns (currently limited to 3-5 microns by the cold filter and imaging lens), and externally triggerable sampling. The procured system includes a 400-MHz Dell Optiplex (s/n UGJB8) computer that controls the camera and 2- channel readout electronics with 14-bit A/D Converters (digital board SBF1064 sn J0068, analog board SBF1065 sn H0066). The computer is equipped with 768 Megabytes of RAM to accommodate DMA of a full delay scan, a 9.1-GB Ultra wide SCSI II Hard drive, framegrabber (s/n PCI9486 & DIG-D5270), and software. The camera control software runs as a Windows application for which no source code is provided, limiting our ability to integrate other functions into the camera control system. Camera procurement was facilitated by contributions from a parallel project at SSEC that would benefit from experience with test data from the PIFTS breadboard. The project is part of the NASA LaRC Advanced Geostationary Studies Program for developing an imaging FTS for temperature and water vapor sounding for operational weather applications.

Camera system testing revealed a number of problems with the camera electronics and control software, which required two shipments of the camera back to the manufacturer for repairs. After setting up and powering up the camera, it was discovered that one of the two channels was not operating properly (returning 13 of 14 bits of data). The camera was returned to Santa Barbara Focalplane, where a bad solder joint was discovered on one of the electronics boards. The board was repaired and returned to us on 7 May 1999. We also discovered control software problems in which actual integration times and the set and displayed integration times did not agree, making it appear that the camera was non-linear. With corrected software the camera appears to be linear up to the point of saturation.

In early August of 1999, while testing trigger generation software (using simulated interferometer scan timing data), problems were discovered in the external trigger functionality of the SBF camera system. The problems caused some frames to be missed, and some to be overexposed, depending on the frame rate and duty cycle of the trigger pulse train. The camera was returned to Santa Barbara Focalplane on 7 August 1999 for problem diagnosis. It was

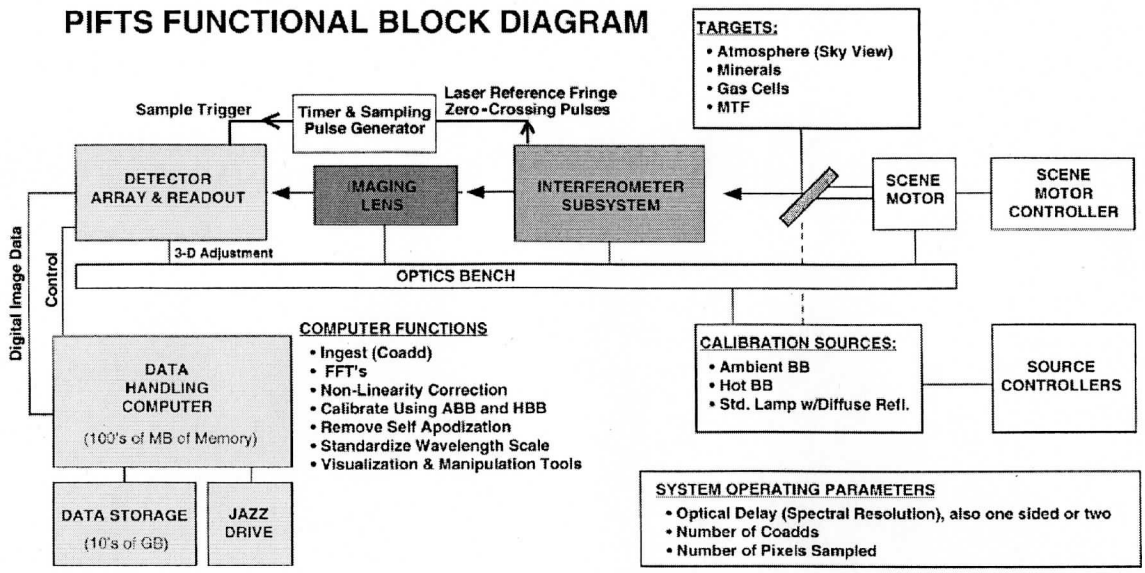

Figure 1: PIFTS breadboard functional block diagram

determined that the external trigger circuitry on the analog electronics board was faulty. We were also informed of a discrepancy between the external trigger specification and the actual implementation, resulting in more stringent triggering requirements. On 18 August 1999, the camera was returned to us, and thereafter it has operated properly in response to external triggering.

3 Breadboard Design

3.1 Overview.

The PIFTS breadboard instrument currently consists of (1) a miniature interferometer subsystem, (2) a dewar-mounted InSb detector array with readout electronics and a camera control computer, (3) a standard IR imaging lens, (4) an optical bench that holds the subsystems in alignment, (5) timing and triggering electronics, and (6) external sources for testing system performance. The functional relationships of these components are illustrated in Fig. 1. Shaded blocks indicate components procured from commercial vendors. The lightest shading indicates the camera system, with darker shades marking the Bomem interferometer and the camera lens. The remaining elements were either borrowed or designed and fabricated at SSEC. The scene mirror, blackbody sources, standard lamps, and controllers are elements that we borrowed from other SSEC projects.

The interferometer package and the camera system are illustrated in Fig. 2. The small box on the left is the Bomem interferometer package, which is 5 in $\times$ 5 in $\times$ 3.5 in. The dewar on the right contains an InSb detector array, and has a commercial IR camera lens (black housing) attached on the interferometer side, and a readout electronics package attached on the right. Other support electronics and calibration hardware are illustrated in Fig. 3.

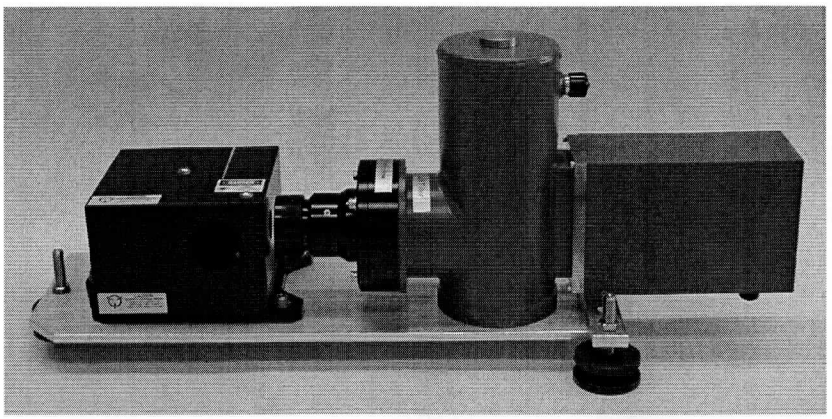

Figure 2: PIFTS modules from left to right: interferometer assembly (box), lens, detector dewar, and readout electronics, mounted on aluminum plate.

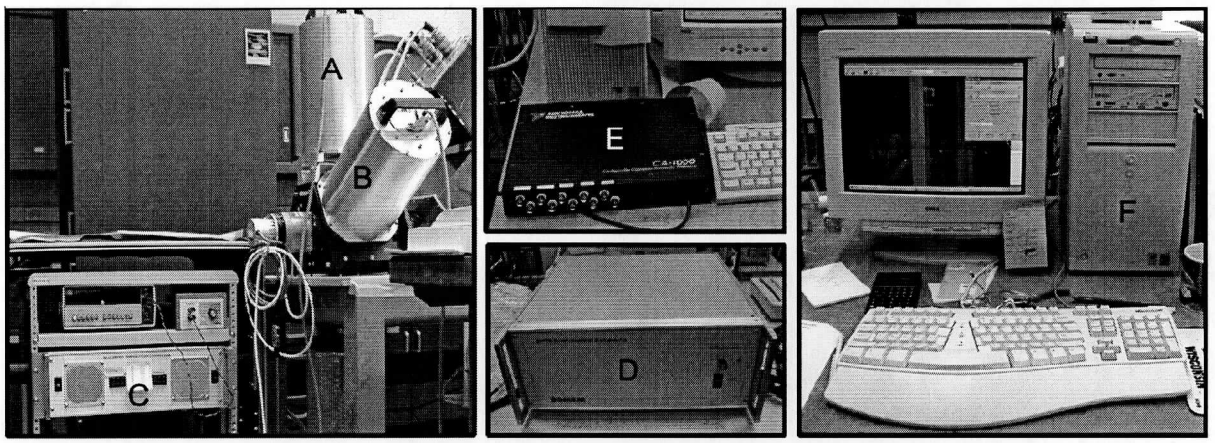

Figure 3: PIFTS support electronics: Heated (A) and ambient (B) blackbody cavities, blackbody controller (C), interferometer scan drive and metrology electronics (D), timer/controller board (E), and camera control computer/data system (F).

3.2 Interferometer design.

The details of the interferometer design are illustrated in the photo and drawing in Fig. 4. The input beam enters through an aperture on the left face, is divided into two beams by a CaF_2 beamsplitter (mounted at 45° to the input axis), which are recombined after reflection from the two corner cubes, exiting near the bottom left (at 90° to the input). The shaded wishbone supports the two corner cube reflectors that provide differential delay scan when the wishbone pivots under control of the two voice-coil drivers. In a standard Michelson configuration, there is one fixed mirror and a second movable mirror to produce an optical path difference between the two beams that are later recombined. Our technological approach has two advantages over this standard approach: (1) the use of corner cubes removes the need for precise alignment of the mirrors, and (2) the use of a wishbone pivot doubles the delay difference for a given mirror displacement, thus making possible higher spectral resolution in a smaller volume. This makes for a more robust and compact instrument. We chose hollow corner cubes to minimize mass. The optical delay is measured by monitoring the fringe intensity of a diode laser, using

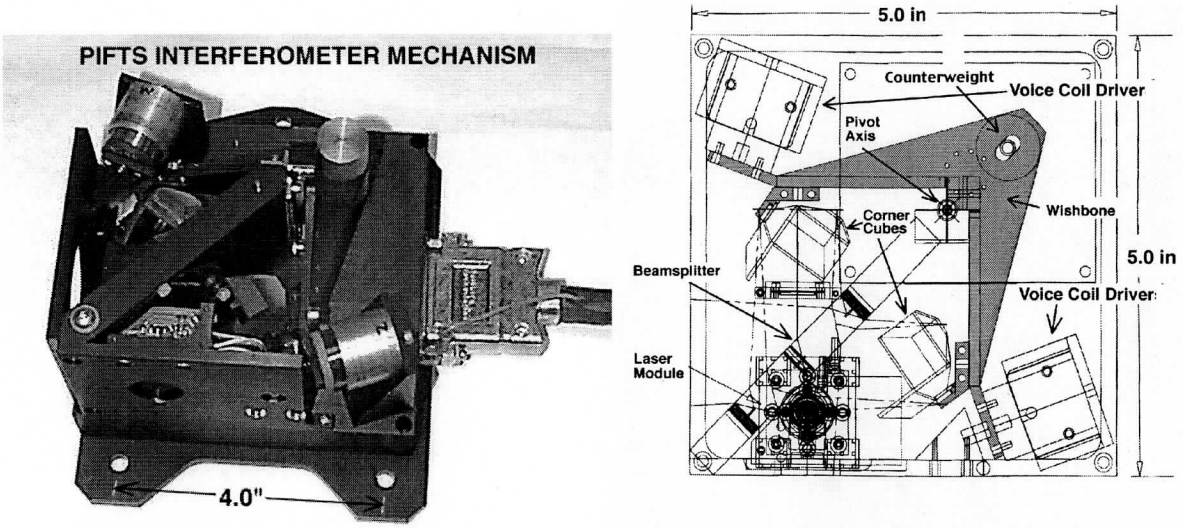

Figure 4: PIFTS interferometer assembly interior mechanism photograph (left) and mechanical drawing top view (right), for which the input from the scene is at the left and the output to the lens is at the bottom.

a retarder plate on one path so that detectors with polarizers can keep track of absolute fringe counts in either scan direction. The scan drive system uses the detected laser fringe signal as feedback to maintain a constant delay scan and to provide zero crossing pulses that are used to control the camera integration timing.

Key interface issues affecting the design of the interferometer system were: (1) optical delay scan rates that were needed by the interferometer scan drive in comparison with the maximum possible image frame rate of the camera readout system, (2) triggering of detector integration timing using interferometer reference laser fringe measurements, and (3) vignetting of the camera lens FOV by interferometer components.

At its highest resolution, the data volume produced by PIFTS is substantial. For our laser wavelength of 852 nm (11,737 cm^{-1}) and two samples per fringe (one at upward zero crossing and one at each downward crossing), the max optical delay scan from -0.4 cm to +0.4 cm generates 18,779 frame synch pulses per double-sided interferogram. For 64×64 pixels and two signal bytes per pixel, we obtain 153.8 MB of image data per scan. At a scan rate of 500 laser fringes/sec (1000 image frames/sec), the 0.8-cm scan takes 18.79 seconds and provides a maximum unapodized spectral resolution of $1/(2\times0.4\text{ cm}) = 1.25\ cm^{-1}$, corresponding to very respectable resolving powers of 4000 at 5 μm, and 20,000 at 1 μm. For most applications resolving powers of a few hundred to a few thousand are needed, implying much shorter delay scans, lasting only a few seconds.

Ray-tracing analyses were used to constrain both our lens choice as well as sizing and arrangement of the internal interferometer optics. The expanding field of view of the camera system through the interferometer is illustrated in Fig. 5, which displays an unfolded linear diagram of the optical layout, with rays indicated for edge and corner pixels of the detector. The optical element positions, diameters, and beam sizes are given in the following table, all in inches.

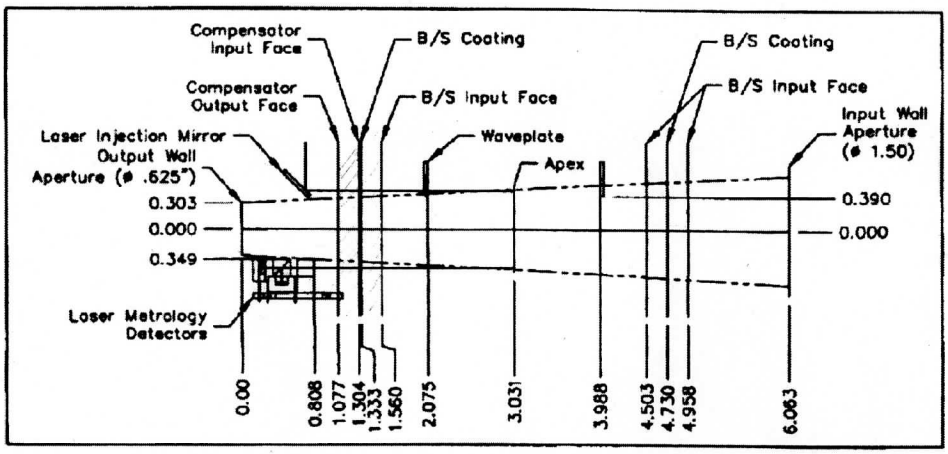

Figure 5: Interferometer unfolded optical layout showing beam expansion and component distances.

Description	Diameter	Location	Space to Next	Beam Size
Output Wall Aperture	0.625	0	0.808	0.606
Laser Line Filter	0.4	0.808	0.269	0.694
Compensator Output Face	2	1.077	0.227	0.723
Compensator Input Face	2	1.304	0.029	0.748
Beamsplitter Coating	2	1.333	0.227	0.751
Beamsplitter Input Face	2	1.56	0.515	0.775
Retardation Plate	0.4	2.075	0.956	0.831
Corner Cube Apex	1	3.031	0.957	0.935
Retardation Plate (Folded Beam)	0.4	3.988	0.515	1.039
Beamsplitter Input Face	2	4.503	0.227	1.095
Beamsplitter Coating	2	4.73	0.228	1.119
Compensator Output Face	2	4.958	1.105	1.144
Input Wall Aperture	1.5	6.063		1.264

A relatively large beam-splitter is used to accommodate the expanding FOV of the imaging lens. Even so, this design has 1/4 the volume of the commercial instrument. There is a small amount of vignetting within the 64X64 detector region. This analysis leaves out the vignetting of the second interferogram that is created by radiation entering from the direction opposite to that of the scene radiation. If the optical system had expanded in both directions from the beamsplitter, and the aperture of the lens were sufficient to admit that large a beam, then the second interferogram would be formed mainly from the cold finger on which the detector is mounted. But in our configuration there is only a small region in which the backward interferogram actually is formed from the cold finger radiation (plus whatever reflects off the optical elements). The outer part of the field of view actually sees background radiation emitted from the lens mount and the interferometer case. This can be seen in the image displayed in Fig. 6.

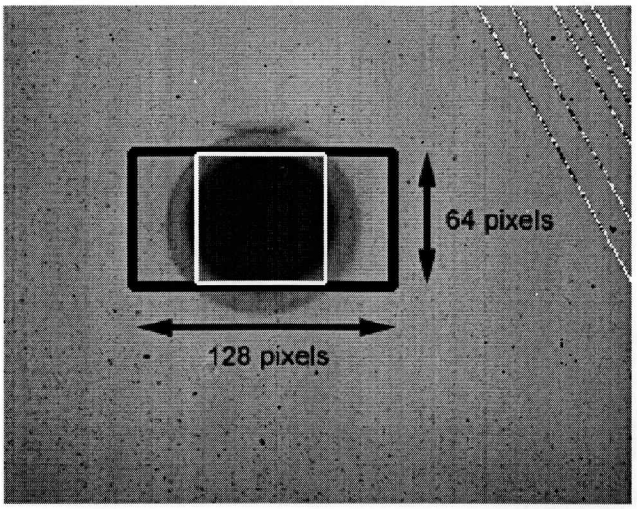

Figure 6: Image of background levels within the pifts field of view. The smallest dark circular region is one in which the rear entering signal arises from the cold finger, in the next annulus the scene is unvignetted, but the rear entering signal arises from apertures at room temperature, within the lens and interferometer, the outermost region contains no scene information, only ambient background contributions. In this view the lens is focussed on the interferometer input aperture. Somewhat different and more blurred patterns apply when focussed on the scene. It should be noted that most blemishes appearing in this image are absent in calibrated images.

3.3 Imaging detector array.

The detector array and readout electronics were purchased as an integrated IR camera system from Santa Barbara Focalplane. As noted previously, the camera uses an InSb array of 320×256 pixels, providing a 128×128 subarray of 99.5% operable pixels, snapshot readout at 60-Hz frame rates, adjustable windowing to 128×64 and smaller subarrays that can be read at > 1 kHz frame rates, a user replaceable cold filter, detector response from 1-5 μm (currently limited to 3-5 μm by the cold filter and imaging lens), externally triggerable sampling, and 2-channel readout electronics with-14 Bit A/D Converters. A read noise of 400 electrons is claimed to be possible, but with the multiplexer included with our detector, and at the high read rates we needed for interferometer compatibility, we obtained a read noise of ~2400 electrons. Detector elements are positioned on a 30-μm square grid, with each element isolated by 3-μm channels, yielding an effective area of 26 μm × 26 μm. This reduces the active-area quantum efficiency of ~89% to an effective value of ~57%. The positive benefit of the isolation channels is relatively low crosstalk (described in a later section).

3.4 The PIFTS delay sampling and triggering system.

Our aim is to provide samples at equal delay intervals throughout each interferogram. The laser metrology system provides the basis for sampling at equal delays. The trigger provided by the interferometer subsystem is a zero crossing pulse. However, if we start sampling at each zero crossing, the end of each integration will delay the average sampling time by half of the integration time. But, because the delay scan drive has small variations in speed, that fixed time delay from the zero reference would lead to variable delay offsets. If we could vary the exposure in accordance with the current speed of the drive, that problem could be avoided.

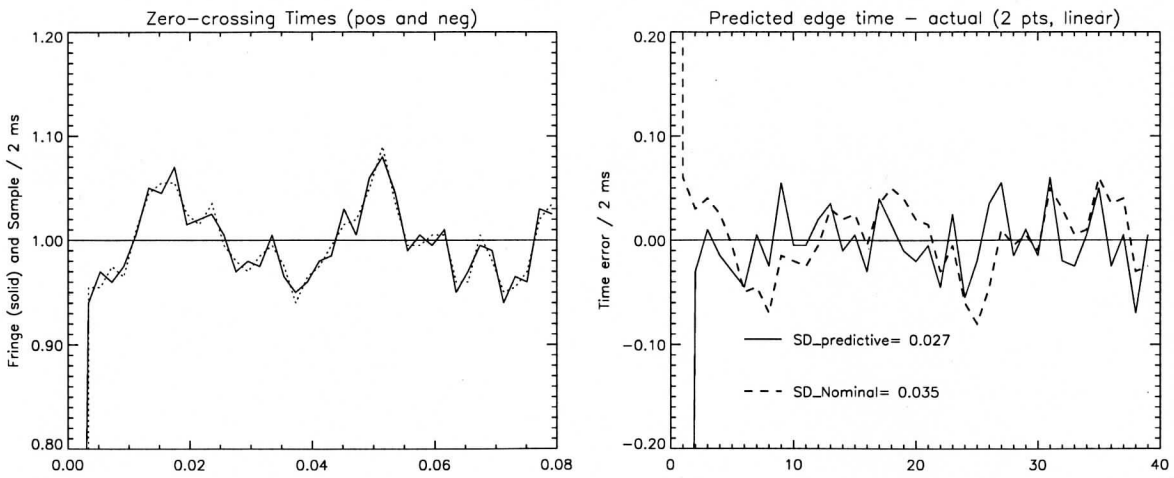

Figure 7: Zero-crossing times (left) as provided by Bomem electronics (solid) and as we computed from laser metrology signals (dotted). Fractional time error (right) if we assume fixed interval (dashed) and if we use predictive correction (solid) with 2-point linear extrapolation as the predictive algorithm.

Given that our system was unable to change exposure times for each frame, we designed a predictive triggering system that could use past zero crossing times to estimate a speed for the next sample, so that the exposure could be started before the next zero crossing by half of the exposure interval. The integration would be started before the fringe zero detection and ended so that the center of the integration is at the time of the zero detection. It is the function of the delay sampling and triggering system to measure the times of the fringe zero crossings, use recent time measurements to predict the next crossing, and then trigger the camera so that the next exposure is centered on that predicted time. This novel sampling scheme, developed for PIFTS at the UW Space Science and Engineering Center, was implemented in hardware using a National Instruments PCI 6602 General Purpose Counter-Timer board (PCI bus) controlled by a separate Pentium computer running under Windows NT, using a C program accessing library subroutines. We tested its effectiveness in reducing sample jitter, with only simple prediction algorithms, and found only minor improvements. An example test result is provided in Fig. 7. The time interval between zero crossing times (left panel) is seen to vary with time, as determined from the laser metrology. The slowest component of that variation has a frequency of about 30 Hz, and should be susceptible to compensation using our proposed scheme. However, using just 4 points, and a 2nd degree polynomial we were able to predict edge times well enough to reduce sample jitter to 0.027 times the 2-ms interval time, while the sample jitter without predictive adjustment would have been 0.035 times the 2-ms interval time. Given the large number of samples per scene fringe at the wavelengths we were using with the current cold filter, we did not feel that the improvement was needed. For shorter wavelengths, the predictive sampling scheme might be considerably more important.

3.5 Imaging optics.

We selected a relatively inexpensive standard commercial lens sold by Diversified Optics: a 25-mm focal length f/2.3 4-element Si-Ge lens limited to operation in the 2-5 μm range by the lens design and materials. Among standard IR camera lenses this lens also provides the maximum

angular FOV (6.22° diagonal) and array coverage (longer focal length lenses have too large an entrance pupil). The physical configuration of this lens is shown in cross section in Fig. 8, and sample ray tracing results shown in Fig. 9. The exit pupil of this lens is located within the dewar, and serves as the cold aperture stop of the system. While this provides a distinct noise advantage, and allows for use of interchangeable lenses, it results in a larger lens configuration than would be preferred for a flight configuration. However, cost considerations precluded our use of a custom lens design. The detector dewar was delivered with a cold stop diameter of 0.525 inches, placed at a distance of 1.03 inches from the FPA, resulting in a slightly larger effective f/# than the lens was designed for (f/2 rather than f/2.3). This may have resulted in a slight reduction in optical quality and possibly slight vignetting, although most of the degradation would likely occur outside the region we used, which is close to the optic axis and of rather small spatial extent compared to the total field coverage of the lens.

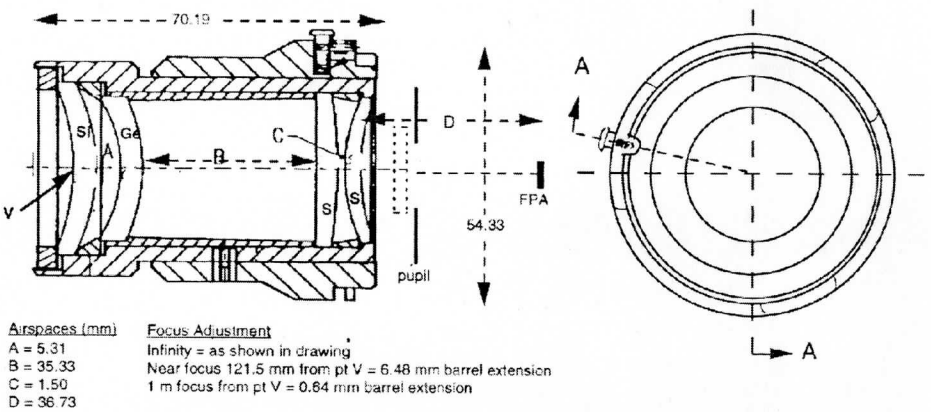

Figure 8: Cross-sectional drawing of imaging optics procured from Diversified Optics: a 4-element 25-mm focal length lens of Silicon and Germanium.

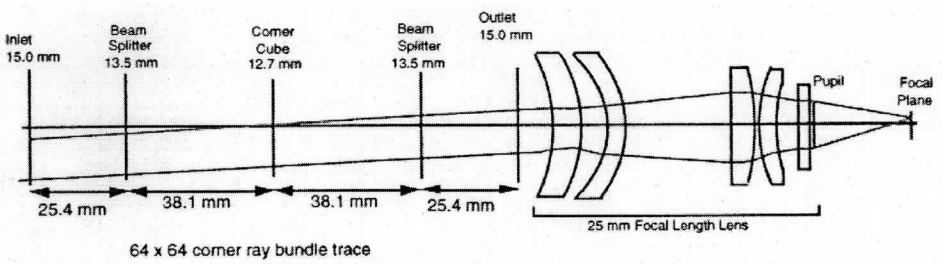

Figure 9: Ray trace diagram of extreme rays from detector through unfolded interferometer.

The selected lens provided a total diagonal field of view of 6.22° on the 64-pixel X 64-pixel subarray. The distance from the lens vertex, V (Fig. 8), to the nearest outer edge of the lens barrel is 8.3 mm. The total motion of the lens barrel from infinity focus to the near focus (121.5 mm) is 6.48 mm. However, if we limit the focusing range to no closer than 1 m, then the total extending motion of the lens from infinity focus to 1 meter focal distance is only 0.64 mm, which is likely as much range as we would ever need. We evaluated vignetting effects assuming a lens barrel to interferometer distance of 3.7 mm to provide some additional margin. With the final interferometer design, the only vignetting that occurs arises from the retardation plate.

This affects only one edge of the detector array, and provides a 4% attenuation at the center of that edge and drops to zero for pixels greater than 7 pixels from the edge. This is a minor effect easily removed in the process of calibration.

An analysis by LMA evaluated the effects of diffraction and chromatic aberrations on the blur circle produced by this lens. With the focus position set to best geometric focus at a wavelength of 4.0 μm, the blur circle contributions from diffraction (Blur diameter D = 1.22 λ f/#) and from geometric blur (diameter G = Δ/(2 f#), where Δ is the chromatic focus shift from 4.0 μm) are root-sum squared so that the total blur diameter B = $(D^2 + G^2)^{1/2}$. The components and total blur are given in the following table.

λ (μm)	D (μm)	Δ (μm)	G (μm)	B (μm)	Energy in 1 pixel	Energy in 2x2 pixels
3.0	8.4	72	15.7	18.1	72%	95%
4.0	11.2	0	0	11.2	85%	95%
5.0	14.0	38	8.3	16.3	77%	91%

The focus shift is seen to be about 55 μm per μm of wavelength shift.

4 Breadboard testing and evaluation.

4.1 Interferometer Scan Drive.

We operated the interferometer scan drive and measured zero crossing times of the laser fringe pattern to evaluate the stability of the servo drive and sampling and triggering system. Typical results are shown in Fig. 10. In a lab environment, we find speed stability to within about 2% if both positive and negative zero crossings are included. If we only look at positive crossings (right pair of plots in the figure), then the stability is about 1.5%, which indicates that a slight offset exists in the zero reference. (A sine wave intersecting with an offset horizontal line will produce uneven spacing between upward and downward zero crossings.) There are sharp peaks in the power spectrum of variations. The peak at 60 Hz is suggestive of power line noise contributions, although that has not been unambiguously determined. Because the servo system itself cannot significantly suppress perturbations above about 100 Hz, large variabilities cannot be present at such frequencies without causing loss of servo lock. A quiet environment, with isolation from vibrations above 100 Hz, is essential for successful servo operation.

The nominal laser wavelength of 852 nm implies an optical delay sampling interval of 426 nm, which yields 11.7 samples per signal fringe at 5 μm and 7.0 samples per fringe at 3 μm. Because the interferometer uses a quadrature system that keeps track of the phase of the reference laser interference pattern, it should be possible to use even more than two samples per laser fringe, which might be desirable when operating the interferometer at much shorter wavelengths (near 1 μm).

4.2 Camera testing.

Readout electronics gain. The gain of the readout electronics is the number of electrons per DN of A/D output. This can be inferred from response to a known radiance source, provided quantum efficiency, and optical throughput are well known. It is also possible to determine gain without that knowledge using the fact that shot noise contributes a variance that is proportional to the number of photoelectrons. If we write the unknown electronics gain

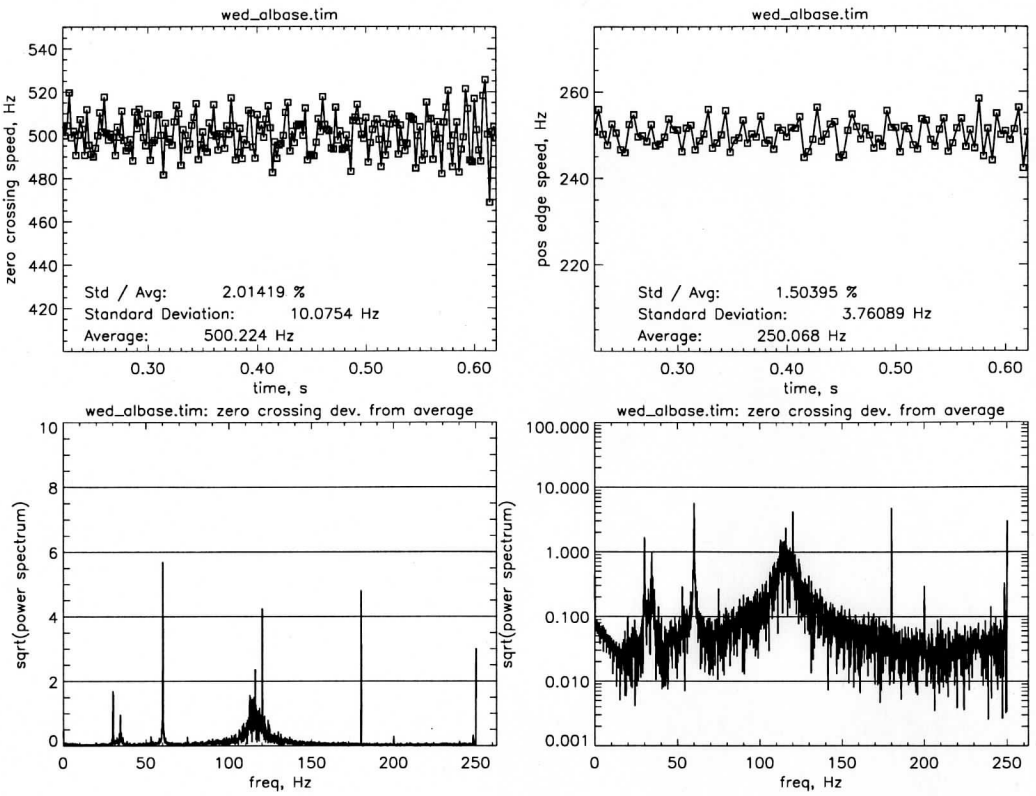

Figure 10: Interferometer scan drive speed variations and sample jitter (upper plots) and power spectral analyses of observed variations (lower plots). The left pair are for both positive and negative zero crossing, and the right pair are for just the positive crossings, which show less variability because they are all shifted the same by an offset in the zero reference. For these measurement no vibration isolation mounts were used.

as G, the number of photoelectrons as n_{pe}, and specific noise contributions ϵ_{pe} for error in the number of photoelectrons and ϵ_{read} for the read noise in electron units, then the total DN for one specific observation can be written as

$$DN = (1/G)(n_{pe} + \epsilon_{pe}) + (1/G)\epsilon_{read} + DN_o \tag{1}$$

where DN_o is an unknown offset. For a large ensemble of such observations the variance will be given by

$$\sigma^2_{DN} = (1/G^2)E[\epsilon^2_{pe} + 2\epsilon_{pe}\epsilon_{read} + \epsilon^2_{read}] = (1/G^2)[\sigma^2_{pe} + \sigma^2_{read}] \tag{2}$$

where $E[x]$ is the expectation value of x, and the mean value becomes

$$< DN >= (1/G)(n_{pe} + DN_o) \tag{3}$$

Using the relation $\sigma^2_{pe} = n_{pe}$, we can write

$$\sigma^2_{pe} = G(< DN > -DN_o) \tag{4}$$

which finally leads to the relation

$$\sigma^2_{DN} = (1/G)(< DN > -DN_o) + \sigma^2_{read}/G^2 \quad (5)$$

which shows that the variance of the ensemble DN is proportional to the ensemble average DN, with the proportionality constant (1/G), which thus allows us to determine the gain merely from the slope of DN variance vs DN. Applying this technique to observations at three different flux levels leads to a gain estimate of 1474±22.8 electrons/DN (Fig. 11). This gain value is within is about 25% higher than the gain determined from estimated throughput and known input radiances (see Fig. 12). This disagreement is larger than expected, and may mean that our witness samples do not accurately represent our actual optical component characteristics. There is further indication of that possibility in the subsequent comparison of spectral responsivity models with measurements (see Fig. 13). This gain estimate using the observed DN variation relative to predicted electron counts uses the entire spectral band of the optical system, and is thus sensitive to uncertainties in cut-off wavelengths. A better comparison would make use of narrow-band filters. Our gain estimate based on DN variance vs DN is about 8% larger than the 1368 electrons/DN inferred from electronics specifications (Table 4.3).

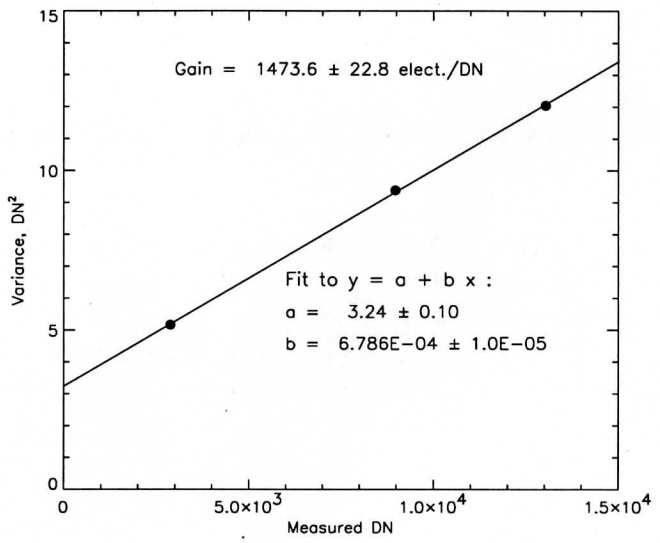

Figure 11: Determination of electronics gain from the slope of DN variance versus DN.

Camera responsivity and linearity. The main camera performance tests were (1) response vs. exposure time for a constant source and (2) response vs. computed in-band flux for three different source temperatures. These tests show that the camera is linear with respect to exposure time up to saturation, with no indication of responsivity curvature, even near the saturation point. Using an improvised calibration assembly consisting of two high-emissivity cavity blackbody references (running at ambient and 40° C) and an LN2 blackbody with a rotating scene mirror for switching camera views, we measured the detector response to source flux, where we computed the incident photon flux on the detector from the source emissions as modified by known atmospheric and component transmissions. We found the camera response to be a linear function of blackbody source flux (within 0.14%, as indicated in Fig. 11, right panel). At 1.3E4 DN we obtained a standard deviation of 3.46 DN, or a S/N of 3750:1 for a nearly full scale signal. For the standard gain configuration we measured 1474±23 electrons/DN

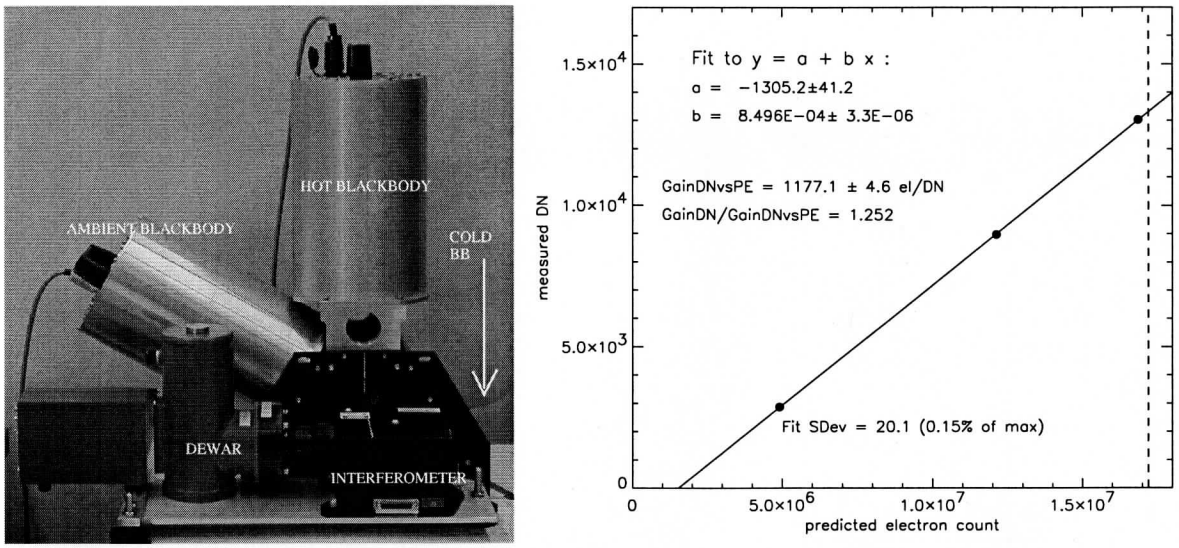

Figure 12: Calibration configuration for complete system (left) and DN vs predicted electron count for system minus interferometer (right). The cold LN2 blackbody (left) is directly below the hot blackbody and not visible in the figure.

(Fig. 12), and a well depth of about 1.6E7 electrons. Read noise was found to be ~2400 electrons. These results were obtained with the standard 3-5 μm dewar window. Additional testing was carried out to establish background contributions from various optical components in the system.

External triggering. Externally triggered sampling was tested at a frame rate of 300 Hz, triggered at 250 Hz, using DMA capture of 5000 128×128 frames (150 MB) in 20 seconds. Saving the image cube to disk took about 30 seconds. Using the IDL FFT routine, it took 1 minute 47 seconds to carry out FFTs for 4096 128×128 frames. This is a data volume about half that of the standard mode in which we use a sub-array of 128×64 pixels, two signal bytes per pixel, that leads to 307.6 MB of image data per scan.

4.3 System-level tests.

The PIFTS breadboard was tested on the system level in two ways. We first measured the spectrum of an ambient blackbody relative to a cooled and heated blackbody. The results are shown in Fig. 13. Second, we made spectral cubes looking out the window of our lab in Madison Wisconsin and at sample minerals.

Radiometric Calibration. In all cases the instrument is calibrated with two blackbodies, one at 40° C, the other at liquid N_2 temperature. Raw two-sided interferograms of each source are collected over the optical delay range from -X to +X, where X is the maximum optical delay. These are fourier-transformed to complex spectra, then initially used in the following equation (Revercomb et al. 1988b) to obtain calibrated radiances:

$$L_\nu = Re\Big[\frac{C_\nu - C_{c,\nu}}{C_{h,\nu} - C_{c,\nu}}\Big](B_\nu(T_h) - B_\nu(T_c)) + B_\nu(T_c) \qquad (6)$$

where $B_\nu(T_c)$ and $B_\nu(T_h)$ denote Planck spectra for cold and hot blackbodies, $C_{c,\nu}$ and $C_{h,\nu}$ the corresponding raw measured spectra (complex), and C_ν and L_ν are the raw complex and calibrated real scene spectra, respectively. Here $Re[C]$ denotes the real part of C. Actually, if the measured spectra were noise free, the ratio in Eq. 6 would be real. The only reason to take the real value is to eliminate the complex contributions produced by noise. The above equation is only approximate because it assumes that all sources have unit emissivity. If we assume that source emission is actually given by

$$L_{\nu,source} = \epsilon_{bb} B_\nu(T_{bb}) + (1 - \epsilon_{bb}) B_\nu(T_a) \tag{7}$$

where ϵ_{bb} is the blackbody source emissivity, T_{bb} is the source temperature, and T_a is the effective emitting temperature of the ambient environment, then Eq. 6 is transformed into

$$L_\nu = Re\Big[\frac{C_\nu - C_{c,\nu}}{C_{h,\nu} - C_{c,\nu}}\Big]\Big[\epsilon_h B_\nu(T_h) - \epsilon_c B_\nu(T_c) + (\epsilon_h - \epsilon_c) B_\nu(T_a)\Big] + \epsilon_c B_\nu(T_c) + (1 - \epsilon_c) B_\nu(T_a) \tag{8}$$

The AERI blackbody cavity sources we used for calibration have an emissivity of 0.9976 (H. Revercomb, personal communication, 5-21-99). The LN2 blackbody cavity we used has an estimated emissivity of 0.9861, computed as 1 - 0.005 (black paint reflection reduced from 4% by cavity enhancement) - 0.00866 (LN2 reflectivity at normal incidence using r = ((n-1)^2/(n+1)^2) with n=1.2053). With these emissivities, using LN2 as a cold reference, and a hot source at 40° C, the use of Eq. 8 instead of 6 produces an increase of ~0.1 K in effective emission temperature for an ambient source. When two AERI cavities are used for sources, the difference between hot and cold source emissivities can be ignored. When an AERI cavity and an LN2 source are used, the direct emission from the cold source can be ignored, but the emissivity difference term $((\epsilon_h - \epsilon_c))B_\nu(T_a)))$ becomes important.

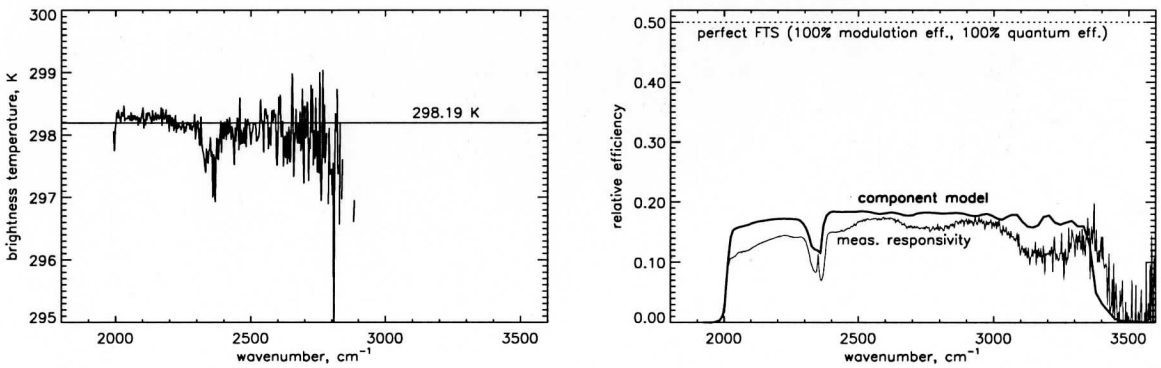

Figure 13: PIFTS spectrum of an ambient blackbody at 298.19 K (left) indicates high radiometric calibration accuracy, while responsivity measurements used to infer system transmission (right) shows that our throughput model based on generic component data (smooth curve) needs improved knowledge of individual optical properties and gains. The 50% transmission line (dotted) is for a perfect FTS with no optics losses, 100% modulation efficiency, and 100% quantum efficiency. The measured responsivity is scaled by a factor of two to account for half of the power residing at negative frequencies.

The intermediate steps in the calibration process are illustrated in Fig. 16, where the raw image shows the pixel-to-pixel variations in camera sensitivity and the uncalibrated FFT image at 2200 cm^{-1} shows the effects of background offset variations over the field of view. In the final calibrated image these effects are accurately removed as part of the calibration process.

Calibration Noise. Our standard practice has been to compute calibration coefficients for each array pixel at each wavelength using just one spectrum each of hot and cold sources. In this case, if the standard measurement error in a single raw spectrum is σ_r, then the standard error in the calibrated scene radiance σ_s can be inferred from Eq. 6. The result is

$$\sigma_s^2 = \sigma_r^2[1 + (1 + \frac{L_s - B_c}{B_h - B_c})^2 + (\frac{L_s - B_c}{B_h - B_c})^2] \tag{9}$$

where B_h and B_c denote the hot and cold source radiances, and L_s is the scene radiance. This equation shows that calibration error usually provides a significant contribution and in some cases can be larger than the error in the raw scene spectrum. Some special cases of note are as follows:

$$\text{For} \quad L_s = 3B_c - B_h \quad \sigma_s = \sigma_r \tag{10}$$

$$\text{For} \quad L_s \ll B_h \quad \sigma_s = \sigma_r\sqrt{2} \tag{11}$$

$$\text{For} \quad L_s \approx B_h \quad \sigma_s = \sigma_r\sqrt{6} \tag{12}$$

It is clear that a substantial improvement in signal to noise can be obtained by improving the accuracy of the calibration. One way is to average a large number of raw calibration spectra. A more efficient alternative is to take advantage of the fact that the main pixel-to-pixel differences in calibration coefficients have only very slow variations with wavelength. One way to take advantage of that characteristic is to carry out a principle component analysis of the pixel-to-pixel variations. Empirical orthogonal eigenfunctions of the covariance matrix provide a set of basis functions which can be used to express the individual pixel deviations from the mean. Because only a small number of functions (those with the largest eigenvalues) are needed to express the real variations, the rest, which are only needed to express the differences due to noise, can be ignored. The result should be a very low noise set of calibration coefficients that will contribute negligible levels of noise to the calibrated scene radiances.

Responsivity. The responsivity of the system is also defined by calibration, according to the relation (Revercomb *et al.* 1988b)

$$R_\nu = |C_{h,\nu} - C_{c,\nu}|/[(B_\nu(T_h) - B_\nu(T_c))] \tag{13}$$

which assumes unit source emissivity. Including the emissivity effects as described above, we obtain the more accurate relation

$$R_\nu = |C_{h,\nu} - C_{c,\nu}|/[(\epsilon_h B_\nu(T_h) - \epsilon_c B_\nu(T_c) + (\epsilon_c - \epsilon_h)B_\nu(T_a)] \tag{14}$$

Some care has to be taken in use of this equation because, the ensemble average of the absolute value of noise is non-zero, which can produce a distortion of the responsivity value at wavelengths for which noise levels are high. In determining an accurate average responsivity for noisy calibration measurements, it is necessary to first average the difference of hot and cold observed raw spectra before taking the absolute value. If responsivities are averaged, noise contributions for regions of low signal/noise will tend to raise responsivity values above their true values.

Our model of system responsivity is a product of optical throughput, detector quantum efficiency, and electronics gain. These factors are summarized in the following table. Spectral curves for several of the components are given in Fig. 14. A comparison of the model with

the measured responsivity is displayed in Fig. 13. While very close agreement is obtained over the 4-5 μm range, in the 3-4 μm range, where noise becomes a much bigger factor, there are substantial discrepancies that remain to be understood. Over the entire spectrum there appears to be a modulation with a period of $\sim$400 cm$-$1, which could be a thin film channel spectrum effect; for an assumed index of 1.4 and normal incidence, the layer thickness would need to be $\sim$9 μm.

Parameter	Value or Curve	Comment
Corner cube transmission	r=0.98[3]	Reflections from 3 gold surfaces
Beam splitter throughput	2RT=0.5	Beam-splitter spec= R, T=0.5$\pm$0.1
Modulation efficiency	56% at 2900 cm^{-1}	Bomem acceptance test measurement
Lens transmission	(Fig. 14)	witness measurements for 3 Si + 1 Ge AR-coated elements
Dewar window transmission	(Fig. 14)	witness transmission from SBFP
Cold filter transmission	(Fig. 14)	witness transmission from SBFP)
Detector QE	0.89 peak	SBFP spectral curve in Fig. 14
Detector fill factor	0.64	SBFP communication.
Electronics gain (May 1999)	1474 el/DN	from Fig. 12 (used in responsivity model)
Nominal electronics gain (2 Aug 2000)	1368 el/DN	FPA gain 5 (133 nV/e) / A/D gain 2 (152.5 μV/DN)

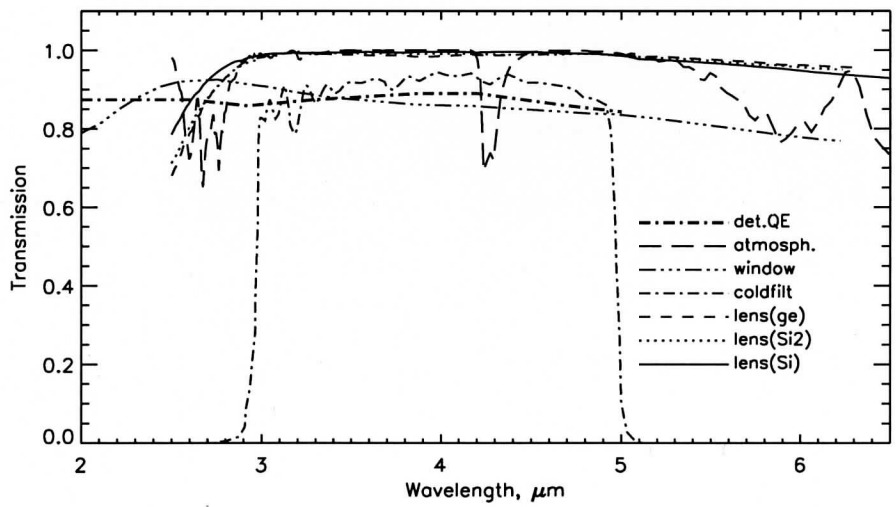

Figure 14: Transmission and quantum efficiency curves for PIFTS optical system components and atmospheric transmission between camera and blackbody references.

4.4 Radiance Noise.

We compute noise equivalant spectral radiance as

$$NESR = \sigma_L = 2X \frac{\sqrt{2}\gamma\sqrt{A_d/2t}}{A\Omega\eta_m\tau D^*} \tag{15}$$

where X is the maximum delay, t is the total time of all interferometer scans, τ is the transmission of the optics (including the loss of 50% of the input beam out the input aperture), A_d is the area of a detector element, $A\Omega$ is the light grasp of the system, η_m is the modulation efficiency, γ is the electronics noise factor, which we will take here to be 1 (i. e., no additional noise contribution) and D^* is the effective specific detectivity of each element of the detector array, computed from the RSS of detector dark current noise, shot noise of background and signal radiation, and read noise. This equation is consistent with Eq. 5.10.2, 5.10.3, and 5.8.14 of Hanel *et al.* (1992), if τ is taken to be their optical efficiency, and $\eta_m/\sqrt{2}$ is taken to be their system efficiency. The modulation efficiency of the PIFTS was measured to be 56% at 2900 cm^{-1}. We expect it to decrease with increasing wavenumber. This arises from wavefront errors associated with deviations from flatness in optical surfaces, for example.

Following the equation of a photon-limited detector (Dereniak and Boreman 1996), in which D^* given by

$$D^* = \sqrt{2}(\eta/(q_b + q_s))^{1/2}\lambda/(2hc) \tag{16}$$

where η is the detector quantum efficiency and q_b and q_s are photon fluxes from the background and scene respectively, we note that the total electron noise variance in flux units (number per unit area per unit time) can be written as

$$\sigma^2_{tot} = \eta \times (q_b + q_s) + \sigma^2_{read}/(A_d t) \tag{17}$$

where A_d is detector area and t is the sample time interval. We compute photon flux from the scene as the source photon radiance times the system transmission τ and detector solid angle of view. The remaining detector view fraction within the same aperture (1 - τ) contains a mix of emissions from the interferometer and from the cold finger. Because we have not carried out the ray tracing necessary to determine the appropriate mixture, we include estimates for the two extremes (all from the cold dewar interior and all from the warm interferometer). For our laboratory configuration, the two extremes do not lead to very different noise estimates (Table III), partly because of the significant contribution of read noise. With lower read noise and lower scene radiances the contribution of interferometer emissions is important in deciding on the benefits of cooling the interferometer.

Table I: System parameter summary for 2 August 2000 lab test.

scan range: -X to +X (X= 0.1740 cm)	OPD scanrate= 0.0213 cm/s
laser wavelength = 852.0 nm	0 - X scan time= 8.169 seconds
fringe rate = 250.0/s	frame rate = 500.0/s (interval = 2 ms)
cold filter transmission= 0.93 (3.00 - 5.00 μm)	detector pitch = 30.0 μm
lens focal length = 25.0 mm	effective lens f# = 2.0
cold aperture stop half-angle = 14.30°	lens half-angle= 14.30°
Total True Photon Flux = 2.5-6.7E+14 phot/cm^2-s	count rate = 1.2-3.3E+09 elect./sec
full well = 1.72E+07 elect.	fill time = 18.85 ms
unapodized resolution: 2.874 cm^{-1}	pixel angular pitch: 1.200 mr
total integration time: 16.17 sec	AΩ: 1.12E-6 cm^2-sr

The effective D^* can then be written as

$$D^* = \sqrt{2}(\eta/\sigma_{tot})\lambda/(2hc) \tag{18}$$

We ignore dark current contributions in comparison with other noise sources because of their negligible size in our applications.

Table II: Summary of photon flux contributions for 2 August 2000 lab test.

Flux Contributor:	cold stop	scene	interferometer	read noise	unit
Temps:	77.00	298.19	293.00		K
Solid angle:	6.14	0.1946	0.1946		sr
Transmission:	1.00	0.3318	0.6682		
Flux:	4.9e+03	2.6e+14	0.0-4.2e+14[a]	5.00e+14	phot/cm^2-s
F/F_{tot}:	0.00	1.000-0.382	0.000-0.618		
$F/(F_{tot}+F_{read})$	0.00	0.34-0.22	0.0-0.356	0.658-0.424	

[a]This range covers the extremes range of interferometer emissions.

Table III: Summary of model D* and noise calculations.

wavelength μm	wavenumber cm^{-1}	D* 10^{11}cmHz$^{1/2}$/W	Noise-Equiv. Radiance mW/m^2-sr-cm^{-1}	NEΔT(298K) K
3.000	3333.33	3.4-2.8	0.029-0.036	11.9-14.6
3.072	3254.90	3.5-2.8	0.029-0.035	8.8-10.7
3.148	3176.47	3.6-2.9	0.028-0.034	6.5-7.9
3.228	3098.04	3.7-3.0	0.027-0.033	4.8-5.8
3.312	3019.61	3.8-3.1	0.027-0.032	3.5-4.3
3.400	2941.18	3.8-3.1	0.027-0.031	2.6-3.2
3.493	2862.75	4.0-3.2	0.026-0.031	1.9-2.4
3.592	2784.31	4.1-3.3	0.025-0.030	1.4-1.8
3.696	2705.88	4.2-3.4	0.025-0.029	1.1-1.3
3.806	2627.45	4.3-3.5	0.024-0.028	0.81-1.0
3.923	2549.02	4.4-3.6	0.023-0.028	0.61-0.74
4.048	2470.59	4.6-3.7	0.022-0.027	0.46-0.56
4.180	2392.16	4.7-3.9	0.023-0.026	0.34-0.42
4.322	2313.73	5.9-4.0	0.021-0.025	0.26-0.32
4.474	2235.29	5.1-4.1	0.020-0.024	0.20-0.24
4.636	2156.86	5.2-4.3	0.019-0.023	0.15-0.19
4.811	2078.43	5.4-4.4	0.018-0.022	0.12-0.14
5.000	2000.00	5.7-4.6	0.018-0.023	0.09-0.11

To validate the performance calculations we measured system noise levels in the laboratory, using measurements of hot (40° C), cold (LN2), and ambient (25° C) blackbodies. The hot and cold observations are used to calibrate the instrument. The derived calibration constants for each detector are subsequently used to compute a radiance for the ambient blackbody, which can then analyzed for noise by taking pixel-by-pixel radiance differences from the mean. These differences contain contributions of hot-bb noise, cold-bb noise, and ambient blackbody noise, as given by Eq. 9.

Measured noise levels for the 2 August 2000 ambient blackbody calibrated radiances measurements are shown in Fig. 15. The delay scan was at a 250-Hz laser fringe rate (0.0213 cm/sec), over a range of $\pm$1.74 mm, for an unapodized resolution of 2.87 cm^{-1}. The noise was computed from the standard deviation of the pixel radiance values in a 17$\times$17 region near the center of the array. The camera exposure time was 1.5 ms compared to a sample time interval of 2 ms. The deduced noise level is generally $\sim$0.075 mW/(m^2-sr-cm^{-1}), but rises significantly in regions where responsivity declines significantly. The relatively constant level is indicative

of dominance by either background shot noise or read noise. In this case read noise is the larger contributor. The model estimate for a single raw spectral measurement is ~0.018-0.036 mW/(m^2-sr-cm^{-1}), and about 1.9-2.0 times larger (from Eq. 9) for a calibrated radiance, which would be ~0.04-0.07 mW/(m^2-sr-cm^{-1}). Thus our model calculations for single measurements (Table III) and observed noise levels for calibrated radiances are in reasonably good agreement, though the observed noise levels tend to be on the high side of the model range, perhaps because of additional noise sources not included in the model. The model does not account for noise increases near the edge of the band due to transmission losses, nor does it account for changing background levels during the interferometer scan (only an average background is subtracted). With better analysis of the calibration observations, using the principal component analysis described previously, we would expect calibrated radiance noise to approach ~0.03 mW/(m^2-sr-cm^{-1}).

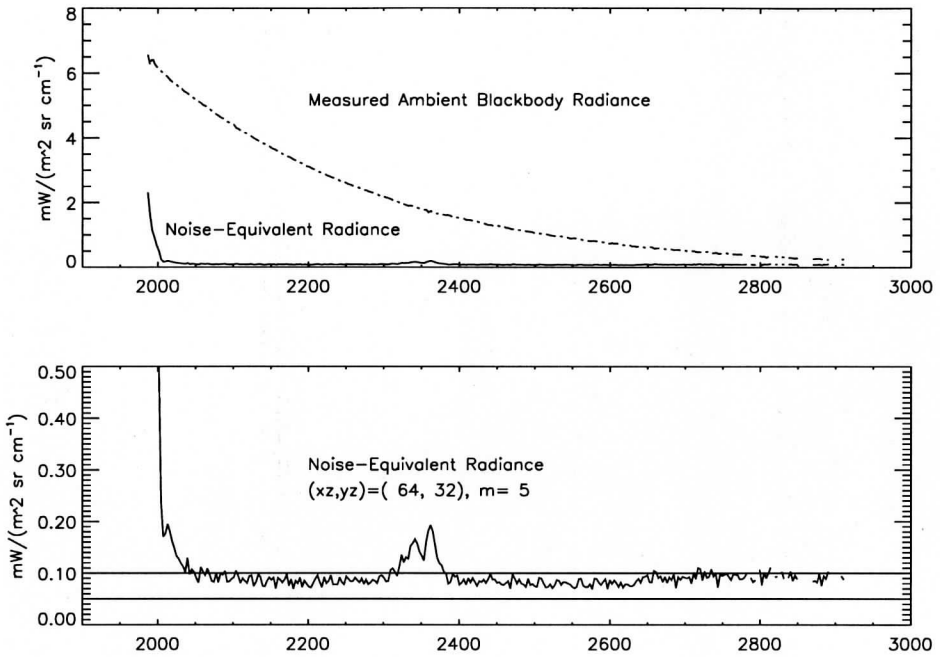

Figure 15: 2 August 2000 measurements of spectral radiance (upper dash-dot) and noise equivalent spectral radiance (upper and lower solid curves). The unapodized spectral resolution was 2.87 cm^{-1}.

4.5 Imaging Downtown Madison.

The sample images in Fig. 16 are from the second system-level test in which we made observations of through an open window in our laboratory. A sample spectrum of one pixel in the scene is provided at the upper right in Fig. 16, where three vertical dashed lines indicate the wavenumbers at which three images are displayed (at 2200 cm^{-1}, 2350 cm^{-1}, and 2500 cm^{-1}). The first of these displays a smokestack and the lake in the background. The second, taken in a strong CO_2 band, doesn't even reach beyond the open window. The third responds to a mixture of emitted radiation and reflected sunlight. In the upper right panel of Fig. 16, the high-amplitude modulations in the spectrum between 2600 cm^{-1} and 3000 cm^{-1} appear as

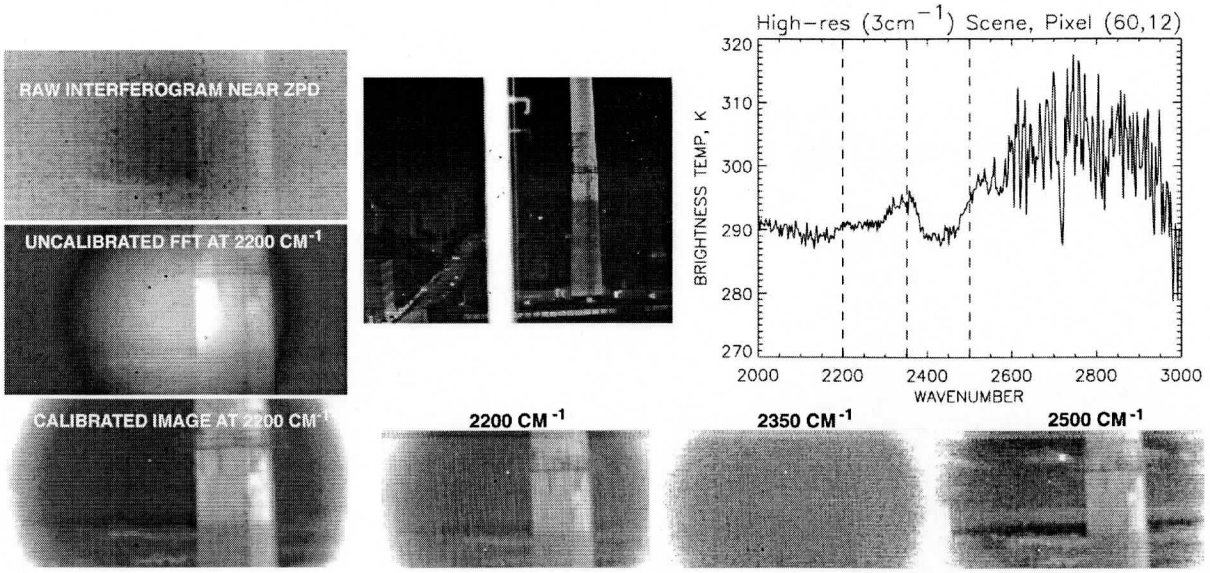

Figure 16: Stages in production of calibrated spectral images (left column) and imaging of downtown Madison (right). The broadband thermal image to the left of the spectrum defines the full 320×256 pixel FOV of the InSb array. (The vertical white bar to the left of the smokestack is the edge of the rotated window frame.) Narrow band spectral images through the interferometer (128×64 pixels), centered slightly left of the middle of the smokestack, are shown at the bottom at 2200 cm^{-1}, 2350 cm^{-1}, and 2500 cm^{-1}. The calibrated spectrum (upper right) is for one pixel positioned on a cloud, as indicated by the white pixel in lower right 2500 cm^{-1} image.

noise, but are actually due to atmospheric absorption features seen in transmission and are used to validate the wavelength scale by comparison to model calculations (described in the next section).

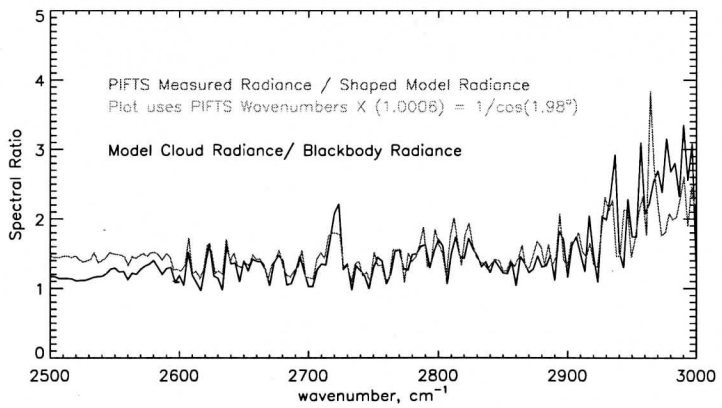

Figure 17: Matching of observed and calculated spectral features by adjustment of the PIFTS wavelength scale. Observed and calculated spectra are divided by smooth reference spectra to reduce slope differences.

4.6 Determination of Wavelength Scale.

Verification of the instrument wavelength scale was made by comparing observed atmospheric spectral features with the corresponding features in calculated spectra (Fig. 17). To match calculated spectra the spectrum from the single pixel displayed requires a factor of 1.0006 multiplication of the nominal pixel scale for on-axis observations. This corresponds to an angle of 1.98° relative to the optic axis. Using cross-correlation between observed and calculated spectra, it should be possible to determine with high accuracy not only the wavelength scale, but the optic axis, and the pixel scale (angular field of view per pixel), the latter two within a small fraction of a pixel.

4.7 Imaging sample minerals.

Mineral discrimination is illustrated by reflectivity images of dolomite and gypsum rocks (Fig. 18) at 3.84 and 4.35 μm, showing dramatic contrast reversal in accord with the spectra in Fig. 19. A quartz-halogen lamp was used to illuminate the rocks.

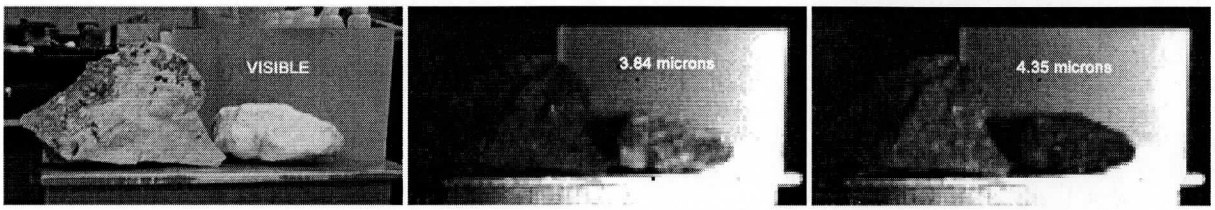

Figure 18: Spectral discrimination of dolomite and gypsum (visible light image at left), using PIFTS spectral data cube image slices at 3.84 μm (middle) and 4.35 μm (right). The dark rock at 4.35 μm is gypsum (see spectra in Fig. 19).

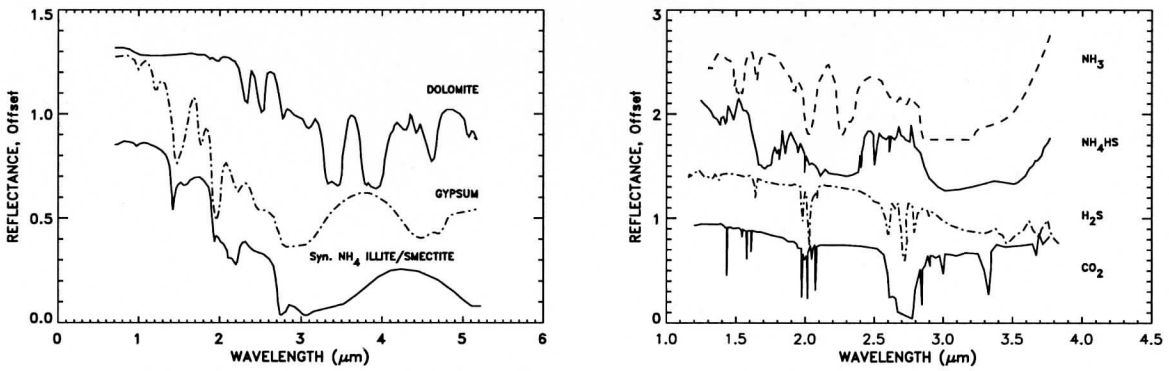

Figure 19: Reflectance spectra of several minerals (left) and frosts (right) at NIMS resolution., from Smythe et al. (1995).

4.8 Measurement of Point Spread Functions (PSF)

A potential problem with detector-array imaging systems is crosstalk between neighboring detectors, through either optical blur or electrical interference, and also possibly between more

distant detectors via multiple reflections. To investigate this issue we measured the Point Spread Function using a bright target of small angular extent that illuminated just one pixel directly. We then looked for crosstalk signals in other detector elements.

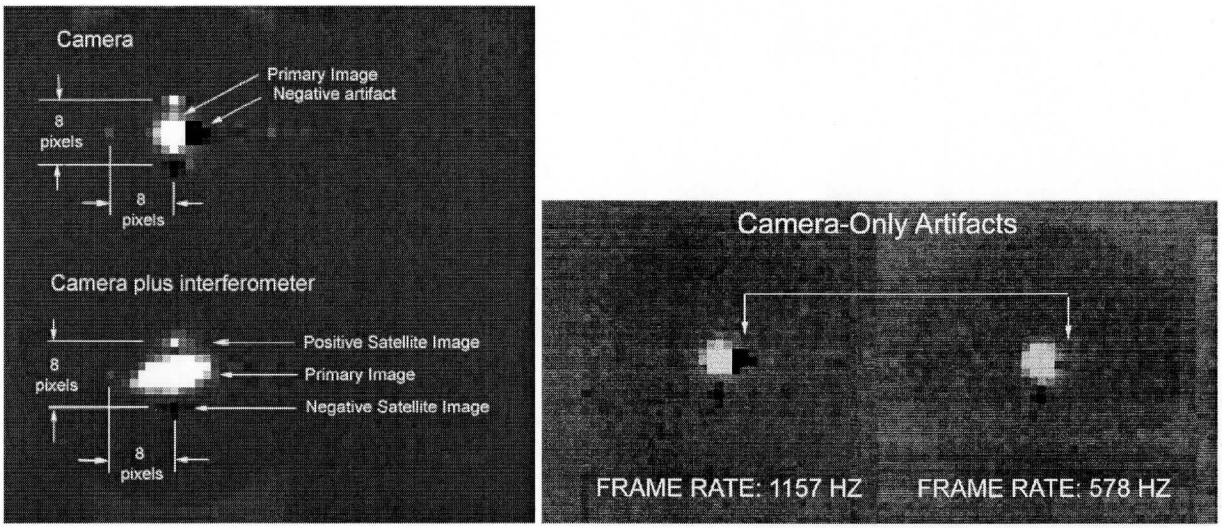

Figure 20: Crosstalk between illuminated and neighboring pixels with and without the interferometer between the camera and the point source (left), and for the camera only, but at two different frame rates (right).

The point-source illuminator was configured using a quartz-halogen lamp behind an aluminum plate with a 1-mm aperture placed at a distance of 74 inches from the camera imaging lens, when the interferometer was in place, and at 71.5 inches when the interferometer was removed. The angular size of the target in these two configurations was 0.45 and 0.47 pixels in diameter respectively, where a single pixel is 1.2 milliradians square.

The point-source imaging results are shown in Figs. 20 and 21. In the left pair of images in Fig. 20 we show a 1000-frame averages to obtain high signal-to-noise ratios. In the camera-only image of this pair (upper), we find a bright central peak of 12000 DN with satellite images 8 pixels above center (100 DN), 8 pixels below center (-100 DN), and ~3 pixels to the right (-500 DN) relative to the coordinates of the main peak. The amplitudes of the artifacts relative to the primary peak are 0.08%, -0.08%, and -4.1% respectively. The comparison between the camera-only and camera+interferometer artifacts shows that the principle artifacts are associated with the camera, and not due to interferometer optical effects, e. g. multiple reflections. In addition, the negative artifacts can not be understood as optical effects. It seems clear that the crosstalk effects are primarily associated with the camera system, and mostly with the read-out electronics. This explanation is further strengthened by the location of upper and lower satellite images exactly 8 pixels apart, and the fact that the size of the largest artifact is strongly dependent on frame rate (shown both at the right in Fig. 20 and also in perspective wire-frame plots in Fig. 21.

Every 4th row in the array is read out by the same set of 320 column amplifiers. Thus, the same amplifier is used to read the primary peak, and the pixels recording satellite positive and negative peaks in rows 4 pixels above and below the primary. It is not clear, however, just what kind of perturbation could affect both preceding and successive readouts. It seems more likely that there is a leakage in mux switches than that there is a time dependence effect, though that is highly speculative at this point. There are two video channels that are created: one carries

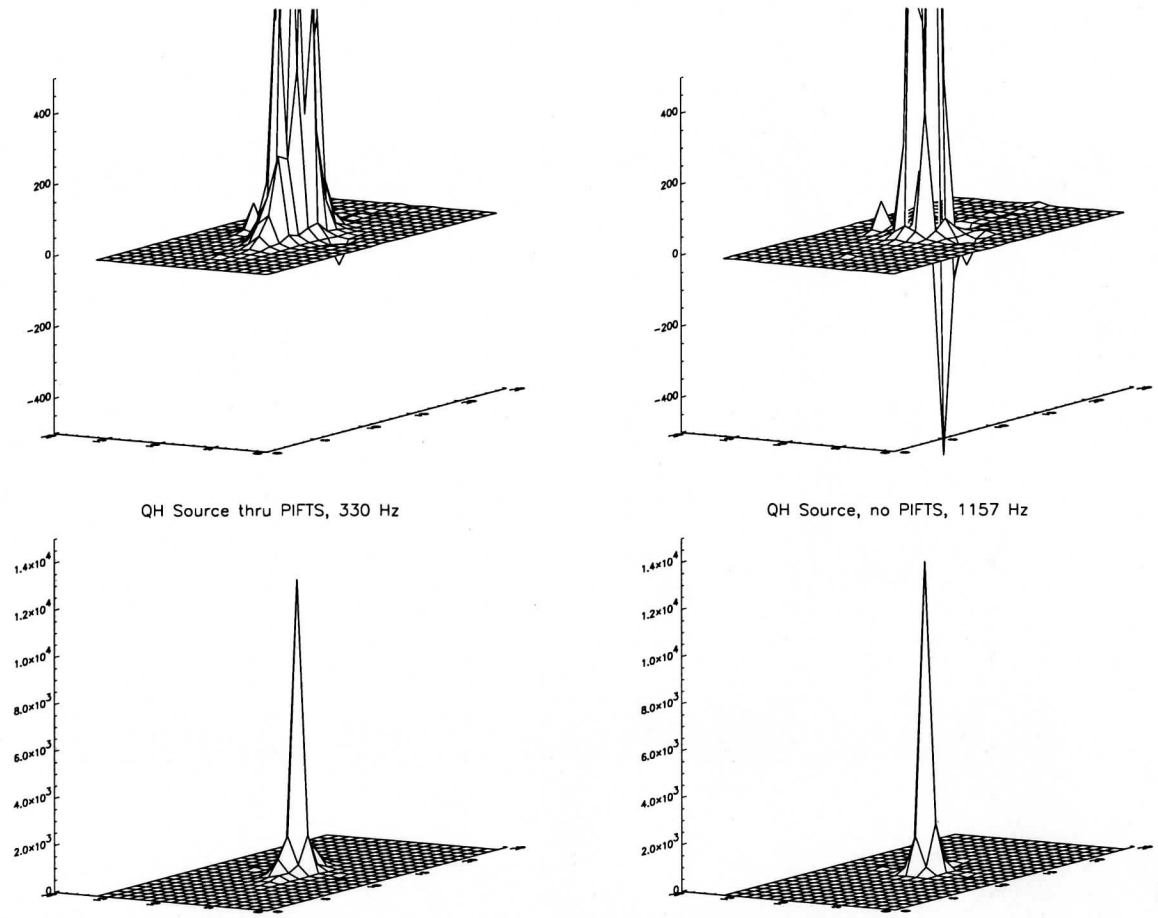

Figure 21: PSF plots for PIFTS + Camera at 330-Hz frame rate (left), and for the camera only at 1157-Hz frame rate (right). In both cases the upper plots are vertical blow-ups of the lower plots.

even column values and the other handles odd columns. The left-right crosstalk patterns are understood even less than the up-down pattern.

There is a difference between the central peak seen with the camera only and that seen with the interferometer in place. As evident from the plots in Fig. 21, the wings of the PSF are broader with the interferometer in place. This may account for the absence of a negative satellite in the PIFTS PSF. It may be filled in by the broader wings of the central peak.

5 Publications and Presentations.

Our work on development of the PIFTS instrument was communicated via two conference presentations and their proceedings:

Revercomb, H.E., L.A. Sromovsky, P.M. Fry, F.A. Best, and D.D. LaPorte (2000) Demonstration of Imaging Fourier Transform Spectrometer (FTS) performance for planetary and geostationary Earth observing. *SPIE 2nd International Asia-Pacific Symposium on Remote Sensing of Atmosphere, Enviroment, and Space*, 9-12 October 2000, Sendai, Japan.

Sromovsky, L.A., H.E. Revercomb, and P.M. Fry (2000) Preliminary evaluation of a Planetary Imaging Fourier Transform Spectrometer (PIFTS). *Proceedings of the Fifth Workshop on Infrared Emission Measurements by FTIR*, held on 9-11 February 2000, ABB Bomem, Quebec, Canada.

6 Possible Modifications to Enhance Performance

6.1 Delay Scan Drive Optimization.

The PIFTS pivoting mirror assembly is driven by a pair of voice coils under closed loop control using a laser metrology system discussed previously. When properly balanced, the wishbone system is inherently insensitive to translational vibrations. However, the imaging interferometer requirements presented challenges to the voice-coil drive system. Because the imaging detector readout rate is limited to 500-1000 Hz (with the readout electronics that we could afford), the optical delay scan must be relatively slow. This made the drive servo more susceptible to lower frequency disturbances. To help deal with this problem, the pivot system was made very stiff, requiring two voice coils and a significant increase in power relative to our initial expectations. Even for a balanced wishbone, twisting vibrations can introduce optical delay perturbations, so that stiffness is a virtue.

The problem with increasing the stiffness of a voice-coil drive using mechanical springs, is that it takes more power to move the mirrors. It should be possible to increase the servo gain sufficiently to achieve the same stiffness as the mechanical spring without even using mechanical spring, thus reducing the power requirements to negligible levels. However, there are limits to how far the gain can be usefully increased because of time delays in the processing of feedback signals, which will ultimately lead to instability at sufficiently high gain. Stiffness achieved by mechanical springs has no associated time delay.

A second alternative is a piezoelectric drive system, which has both high stiffness and low power requirements. Vibration sensitivity is not much of an issue in a vibration-free environment. However, if a mechanical cooler is used, then the delay scan drive must be able to handle the mechanical cooler vibrations. In addition, operation on a planetary surface, in the presence of winds, or on the same platform on which other mechanisms are operated, also requires some degree of vibration immunity. Increasing the scan speed would make it easier to servo, but would require increasing the readout rate. That is possible, but expensive, for a breadboard instrument, and increases power requirements, and may also increase read noise.

6.2 Optimization of Optics

The optical arrangement used in the initial breadboard took advantage of the low cost and high efficiency of a commercial imaging lens designed for interchangeability. The disadvantage of this lens for interferometer applications is the large entrance pupil that results from placement of the cold aperture stop behind the lens. This allows the lens to be warm while the aperture stop is cold, a distinct advantage to earthly uses, but far from optimal for planetary applications, both because of the size of the lens assembly, and the wasted interferometer aperture due to the large entrance pupil of lenses of this type. With a custom design that includes a cooled aperture within the lens assembly a much more compact optical arrangement is possible, and a given interferometer aperture can provide a larger angular field of view than with the commercial lens configuration. To advance towards an optimized instrument a customized optical design would be essential. Besides redesigning for compactness, maximizing spectral coverage will also need

to be accounted for. Panchromatic lenses covering wide spectral ranges are expensive. Low dispersion materials might be considered, such as sapphire, which can be fashioned into lenses in spite of its exceptional hardness. An all reflecting optical system should also be considered for wide-band applications.

6.3 Dealing with Channel Spectra

The beam-splitter and compensator are normally wedged so that multiple reflections are deflected from the main path and do not contribute to the recombined beams. If not wedged, these elements contribute channel spectra(periodic modulations in transmission) at wavenumber spacings that depend inversely on the thickness of the elements, i.e. $\delta\nu = (2n_i d\cos(\theta_i))^{-1}$, where d is the element thickness, n_i is its refractive index, and θ_i is the internal angle of incidence. If the channel spectra are at low enough frequencies to be resolved, then they are removed automatically from calibrated spectra. But if they are at very high frequencies and thus not resolved, their effects can range from negligible to significant, depending on the spectral content of the observed scene. Because of the relatively wide FOV of the PIFTS, we did not find it convenient to use wedged beam-splitters, nor to use thin enough beam-splitters to allow resolved channel spectra. The wavenumber spacing of transmission modulations from various components of the PIFTS are as follows: 9.6 cm^{-1} for the gap between the beam-splitter and compensator, which should have been resolved and seen in the responsivity spectrum but was not seen, 2.04-cm for the 0.040-inch thick dewar window, near the limit of resolution, and 0.71 cm^{-1} for either the compensator or beam-splitter, which is not resolvable. The lack of visibility of channel spectra arising from the beam-splitter gap suggests a possible compensation effect in which transmission losses are somewhat compensated for by reflection gains. Given that the net efficiency of the beam-splitter is the product of reflection and transmission, and that the change in R×(1-R) at R near 0.5 is zero to first order, such modulations might not be easily seen in the responsivity function.

Evaluations of the effects of unresolved spectra are needed. There is no significant effect on spectra that contain no features as narrow as the the unresolved channel spectra. Thus it is only a consideration for atmospheric spectra. The best approach is probably to use thin enough optical elements so that channel spectra can be resolved and thus removed in the calibration process.

6.4 Miniaturization of Electronics

Our work made use of commercial electronics to handle detector readout, A/D conversion, image data processing and analysis, scan-drive.servo control, and blackbody temperature control. A viable flight system must use flight-qualified electronics and a more space- and power-efficient electronics design.

7 PIFTS Science Applications

7.1 Overview of Science Objectives.

The science objectives for the PIFTS instrument are similar to those of the Galileo NIMS instrument (Carlson et al. 1992), which does imaging in a similar spectral range, but with considerably lower resolving power (maximum $\lambda/\delta\lambda$=40-408 at 1-5 μm for NIMS compared to 10,000-1600 unapodized for PIFTS). Both instruments aim to use spectral imaging to map

the composition of geological surfaces by measuring and decoding spatial variations in spectral signatures, to study horizontal morphology of surface composition, and to investigate compositional changes over time, either over relatively short periods such as eruptions on Io, or over relatively longer periods of seasonal change such as changes in Martian polar caps, and even geological periods using correlations of composition with tectonic and volcanic features and crater populations. Measuring the composition of surface minerals on Mars, moons, asteroids, and comets are feasible objectives of such multispectral imaging. Atmospheric scientific investigations are also possible with moderate resolution imaging spectroscopy in the 1 to 5.2 μm spectral range (R. W. Carlson et al. 1993; Drossart et al. 1993), but a much richer bounty of atmospheric information is obtained with resolving powers of several thousand, which can be provided by PIFTS. Orbiting or fly-by spectral imaging in this spectral range could sense the upper level cloud layering of Jupiter or Saturn using scattered sunlight in the near-IR methane bands, or look at the deeper cloud structure using emission spectra in the 5 μm window in the hydrogen absorption spectrum. Atmospheric investigations benefit from higher spectral resolution that facilitates more unambiguous identifications of trace gas compositions, and better vertical resolution of atmospheric structure and gas mixing ratios. By making the instrument design flexible enough to accommodate mirror scan delay increases, resolution can be tuned to the mission objectives.

7.2 Operational and Technological Advantages.

The PIFTS blends established technologies in a new way to provide a versatile, generally useful instrument for hyperspectroscopy. The interferometer itself has only one moving part (a pivoting mirror assembly). The delay scanned method of interferogram recording allows adaptive resolution selection by merely adjusting the delay scan range. A multi-mission capability is thus more easily achieved, as well as adapting to different objectives within a given mission. The concept embodies many of today's virtuous features for spacecraft instruments: it is small, low in mass, has low electrical power consumption. It gathers data at a very high rate by using massively parallel spatial sampling. The PIFTS requires only modest technological development and this work proposes to accomplish much of the development. The use of cube corner retroreflector mirrors and continuous visible light monitoring of path length eases the need for high mechanical repeatability. Wavelength accuracy and radiometric calibration accuracy offer fundamental advantages over competing hyperspectral instrument concepts.

The PIFTS appears promising for obtaining hyperspectral data from a flexible instrument that can be accurately calibrated both in wavelength and radiometrically. The concept lends itself to an instrument made of modules whose development are largely independent. Spectral range, spectral resolution, spatial resolution, detector format and field of view can all be chosen over a range of values as appropriate for a mission. Those variables are not totally independent but they do not interact strongly. Minor variations in construction and operation of the PIFTS can tailor it for a variety of missions without the need to rethink the basic design.

7.3 Potential Applications.

A small, low mass, near-IR imaging spectrometer offers the possibility of a significant science return from low-cost missions, especially when wedded to increasingly powerful computing capability that allows on-board processing so that information images could be returned instead of just masses of spectral image "cubes". With on-board Fourier transforms to yield spectra, it then becomes possible to extract just those spectral ranges relevant for each mission science

objective; examples would include window regions near 1.1, 1.7, and 2.3 μm to probe emissions from different levels in the Venus atmosphere from Venus orbit, 2.2-2.5 μm to study possible scapolite distributions on Mars, or 4.5 to 5.2 μm to study emissions from the 1 to 5 bar level in Jupiter's atmosphere. For some missions where spectral signatures are uniquely separable, the returned data might be just images of compositional type. The near-IR spectral range proposed here is capable of distinguishing mineral compositions expected to be present on planetary surfaces, and thus provide the information needed to make images of the compositional morphology of those surfaces. An example of the diagnostic capability is provided in Fig. 19, adapted from Smythe et al. (1995). In this figure the reflectance spectra of various minerals and frosts are shown at NIMS resolution, illustrating distinctive spectral signatures of these compositional elements that can be resolved by the proposed instrument.

Compositional information, besides answering questions about the current chemical states of the surfaces of solar system objects, also allows the investigation of formation and history of the surface materials by correlating composition with age and geological morphology. How does composition vary with age of the surface as determined by crater populations? How do ejecta from crater impacts differ in composition from background materials? What compositional differences exist between different terrain types? These are clues to formation and evolution of the surfaces. Answers to some of these questions provide a powerful tool for selection of samples for Mars sample return missions. There are a number of H_2O ice features in the 1-3 μm range that have been observed in spectra of the Mars surface (Soderblom 1992) and would be accessible to PIFTS.

A fully developed PIFTS instrument could also contribute significantly to many different kinds of atmospheric investigations. Planetary atmospheres contain many gases with absorption bands within the proposed near-IR spectral range, and also contain windows that allow deeper views of atmosphere and, in some cases, surface features. Visible imaging is limited by Rayleigh scattering to relatively high levels in the atmospheres. Given that Rayleigh scattering cross sections (and optical depth) vary inversely as the fourth power of wavelength, and that optical depth is proportional to pressure, in a clear atmosphere the pressure depth that can be probed at 2 μm is 256 times greater than at 0.5 μm. Even suspended particulate hazes can also be penetrated at longer wavelengths to probe deeper structures. For example, according to the revised model of Toon et al. (1992) the optical depth of Titan's atmosphere at 0.5 μm is about 3 (primarily due to haze), while at 2.1 μm it drops to about 0.06, allowing views of the surface features through 1.6 bars of atmosphere and through the several hundred km of haze that presented a pretty featureless view to Voyager's cameras. Wavelengths in window regions allow views to great depths; nearby wavelengths at which atmospheric absorption features are present allow determination of the vertical locations of clouds.

8 References

Brault, J. W. 1985. Fourier Transform Spectrometry. In *High Resolution in Astronomy*, A. Benz, M. Huber, and M. Mayor, Eds., Geneva Observatory, Sauverny, Switzerland.

Carlson, R. W., et al. (1993) Variations in Venus cloud particle properties: a new view of Venus's cloud morphology as observed by the Galileo Near-infrared Mapping Spectrometer, *Planet. Space Sci.* **41**, No. 7, 477-485.

R. W. Carlson et al. (1992) Near-Infrared Mapping Spectrometer Experiment on Galileo. *Space Science Reviews* **60**, 457-502.

R. W. Carlson et al. (1993) Variations in Venus cloud particle properties: a new view of Venus cloud morphology as observed by the Galileo Near-infrared Mapping Spectrometer. *Planet. & Space Sci.* **41**, 477-485.

Dereniak and Boreman 1996. *Infrared Detectors and System*, John Wiley & Sons, p. 214.

Drossart et al. 1993. P. Drossart et al. (1993) Search for spatial variations of the H_2O abundance in the lower atmosphere of Venus from NIMS-Galileo. *Planet. & Space Sci.* **41**, 477-485.

Hanel, R. A., B. J. Conrath, D. E. Jennings, and R. E. Samuelson 1992. *Exploration of the Solar System by infrared remote sensing*, Cambridge University Press, Cambridge, 458 pp.

Revercomb, H.E., L.A. Sromovsky, P.M. Fry, F.A. Best, and D.D. LaPorte (2000) Demonstration of Imaging Fourier Transform Spectrometer (FTS) performance for planetary and geostationary Earth observing. *SPIE 2nd International Asia-Pacific Symposium on Remote Sensing of Atmosphere, Enviroment, and Space*, 9-12 October 2000, Sendai, Japan.

Revercomb, H.E., W.L. Smith, F.A. Best, J. Giroux, D.D. LaPorte, R.O. Knuteson, M.W. Werner, J.R. Anderson, N.N. Ciganovich, R.W. Cline, S.D. Ellington, R.G. Dedecker , T.P. Dirkx, R.K. Garcia, and H.B. Howell (1996) Airborne and ground-based Fourier transform spectrometers for meteorology: HIS, AERI and the new AERI-UAV, *Proceedings SPIE Optical Instruments for Weather Forecasting* **vol 2832**, G.W. Kamerman, editor, p 106-117.

Revercomb, H.E., W. L. Smith, R. O. Knuteson, F. A. Best, R. G. Dedecker, T. P. Dirkx, R. A. Herbsleb, G.M. Buchholtz, J. F. Short, and, H.B. Howell (1994) AERI - Atmospheric Emitted Radiance Interferometer. *Eighth Conference on Atmospheric Radiation.* Nashville, TN, 23-28 January, p 180-182.

Revercomb, H.E., D.D. LaPorte, W.L. Smith, H. Buijs, D.G. Murcray, F.J. Murcray, and L.A. Sromovsky (1988a) High-Altitude Aircraft Measurements of Upwelling IR Radiance: Prelude to FTIR from Geosynchronous Satellite. *Mikrochimica Acta [Wien]* **II**, 439-444, 1988.

Revercomb, H.E., H. Buijs, H.B. Howell, D.D. LaPorte, W.L. Smith, and L.A. Sromovsky (1988b) Radiometric Calibration of IR Fourier Transform Spectrometers: Solution to a Problem with the High Resolution Interferometer Sounder. *Applied Optics* **27**, 3210-3218

Simons, D.A., et al. (1994) CFHT's imaging Fourier Transform spectrometer, *SPIE* **Vol. 2198**, *Instrumentation in Astronomy VIII*, pp 185-193.

Soderblom, L. A. (1992) The Composition and Mineralogy of the Martian Surface from Spectroscopic Observations: 0.3 μm to 50 μm, in *MARS*, edited by H.H. Kieffer, B.M. Jakosky, C.W. Snyder, and M.S. Matthews, University of Arizona Press, Tucson.

Smythe, W.D., et al. (1995) Galilean satellite observation plans for the near- infrared mapping spectrometer experiment on the Galileo spacecraft. *J. Geophys. Res.* **100, E9**, 18957-18972.

Sromovsky, L.A., H.E. Revercomb, and P.M. Fry (2000) Preliminary evaluation of a Planetary

Imaging Fourier Transform Spectrometer (PIFTS). *Proceedings of the Fifth Workshop on Infrared Emission Measurements by FTIR*, held on 9-11 February 2000, ABB Bomem, Quebec, Canada.

Sromovsky, L.A., J. Hayden, F.A. Best, and H.E. Revercomb (1992) Galileo Net Flux Radiometer Experiment. *Space Science Reviews* **60**, 233-262.

Sromovsky, L.A., J. Hayden, F.A. Best, and H.E. Revercomb (1992) Galileo Net Flux Radiometer Experiment. *Space Science Reviews* **60**, 233-262.

Toon, O.B., C.A. Griffith, and R.P. Turco (1992) A Physical Model of Titan's Aerosols, *Icarus* **95**, 24-53.

Villemaire, A. D., et al. (1995) Imaging Fourier Transform Infrared Spectrometer. *SPIE* **Vol. 2480**, Aerosense '95 Imaging Spectrometry, pp 387- 397.